

SANDIA REPORT

SAND97-0522 • UC-239
Unlimited Release
Printed March 1997

RECEIVED
MAR 20 1997
OSTI

Self-Repairing Control for Damaged Robotic Manipulators

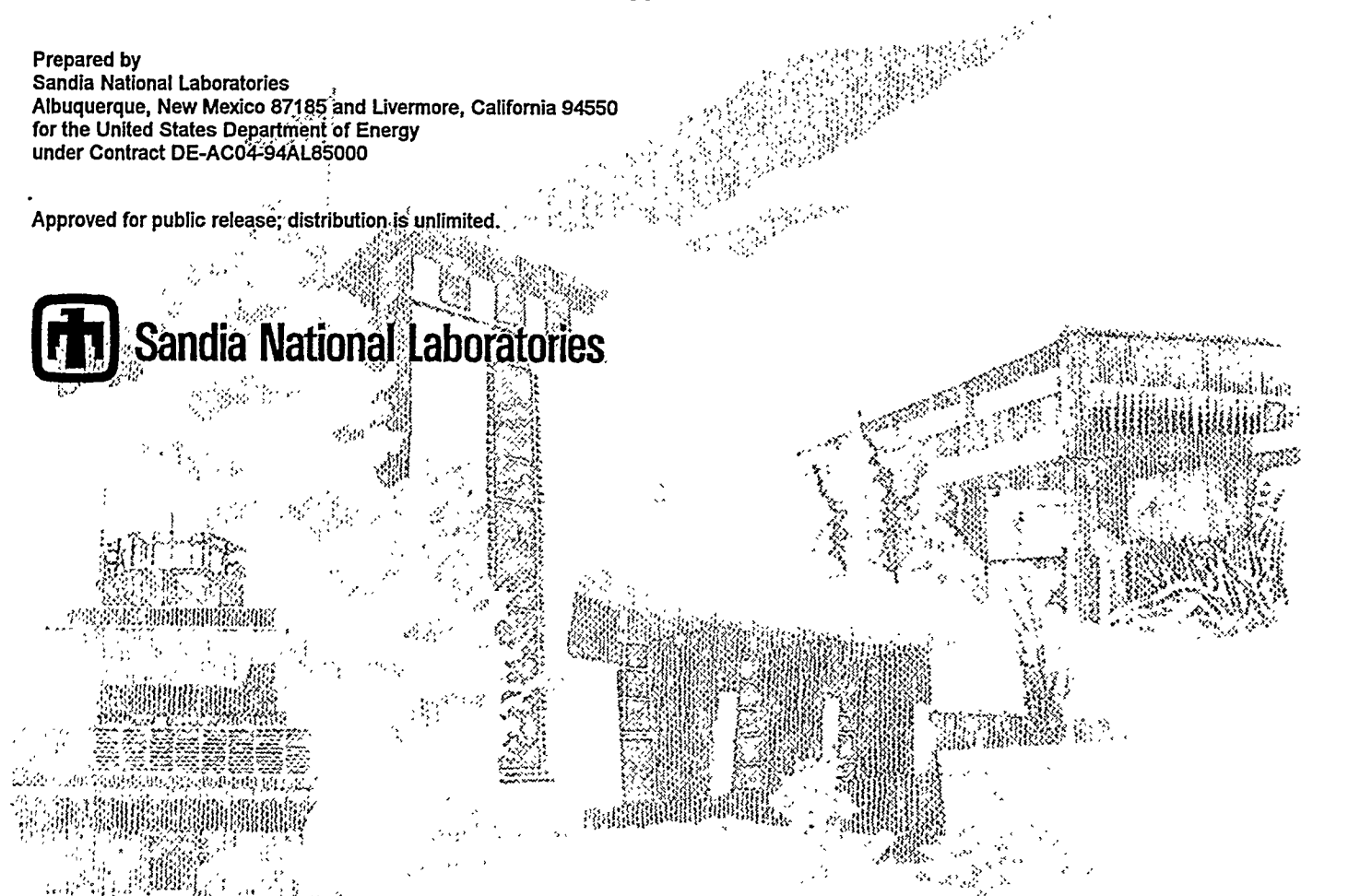
ph
DISTRIBUTION OF THIS DOCUMENT IS UNLIMITED

MASTER

G. Richard Eisler, R.D. Robinett, C.R. Dohrmann, B.J. Driessen, G. Parker

Prepared by
Sandia National Laboratories
Albuquerque, New Mexico 87185 and Livermore, California 94550
for the United States Department of Energy
under Contract DE-AC04-94AL85000

Approved for public release; distribution is unlimited.



Issued by Sandia National Laboratories, operated for the United States Department of Energy by Sandia Corporation.

NOTICE: This report was prepared as an account of work sponsored by an agency of the United States Government. Neither the United States Government nor any agency thereof, nor any of their employees, nor any of their contractors, subcontractors, or their employees, makes any warranty, express or implied, or assumes any legal liability or responsibility for the accuracy, completeness, or usefulness of any information, apparatus, product, or process disclosed, or represents that its use would not infringe privately owned rights. Reference herein to any specific commercial product, process, or service by trade name, trademark, manufacturer, or otherwise, does not necessarily constitute or imply its endorsement, recommendation, or favoring by the United States Government, any agency thereof, or any of their contractors or subcontractors. The views and opinions expressed herein do not necessarily state or reflect those of the United States Government, any agency thereof, or any of their contractors.

Printed in the United States of America. This report has been reproduced directly from the best available copy.

Available to DOE and DOE contractors from
Office of Scientific and Technical Information
P.O. Box 62
Oak Ridge, TN 37831

Prices available from (615) 576-8401, FTS 626-8401

Available to the public from
National Technical Information Service
U.S. Department of Commerce
5285 Port Royal Rd
Springfield, VA 22161

NTIS price codes
Printed copy: A03
Microfiche copy: A01

DISCLAIMER

Portions of this document may be illegible in electronic image products. Images are produced from the best available original document.

SAND97-0522
Unlimited Release
Printed March 1997

Distribution
Category UC-239

Self-Repairing Control for Damaged Robotic Manipulators

G. Richard Eisler, R. D. Robinett, C. R. Dohrmann, B. J. Driessen
Structural Dynamics and Vibration Control Department
Sandia National Laboratories
P.O. Box 5800
Albuquerque, NM 87185-0439

G. Parker
Mechanical Engineering and Engineering Mechanics Department
Michigan Technological University
Houghton, Michigan 49931

Abstract

Algorithms have been developed allowing operation of robotic systems under damaged conditions. Specific areas addressed were optimal sensor location, adaptive nonlinear control, fault-tolerant robot design, and dynamic path-planning. A seven-degree-of-freedom, hydraulic manipulator, with fault-tolerant joint design was also constructed and tested. This report completes this project which was funded under the Laboratory Directed Research and Development program.

Acknowledgment

This work was performed at Sandia National laboratories and was supported by the U.S. Department of Energy under Contract Number DE-AC04-94AL85000 via the Laboratory Directed Research and Development Program.

Summary

Remote operation of a robotic system is a requirement for operation in hazardous workplaces and in contaminated cleanup sites. Robust methods of control are needed that can deal with unexpected changes or damage to the system. The goal of this project was to develop methodologies and software to enable damaged robotic manipulators to reconfigure their control systems autonomously, approximating their original tasks in a hazardous and constrained workspace. This effort lead to the development of off-line analysis techniques for redundant actuator placement, adaptive nonlinear control methods using available sensor information, a redundant robot joint system test-bed, and a nonlinear fault detection and isolation strategy.

Contents

Abstract	i
Acknowledgment	ii
Summary	iii
Contents	iv

Self-Repairing Control for Damaged Robotic Manipulators

Introduction.....	7
Optimal Design	7
Nonlinear Control	11
Path-Planning.....	22
Fault-Detection and Isolation	22
Test-Bed	28
References	28
Appendix A	33
Appendix B	37

Figures

Figure 1 . Case 1, No workspace “hole” minimization	10
Figure 2 . Case 2, With workspace “hole” minimization.	10
Figure 3 . Two mass, nonlinear system.	13
Figure 4 . System response of cg.	15
Figure 5 . System response of relative motion.	15
Figure 6 . Rotating flexible beam system.	16
Figure 7 . Nominal hub angle and tip deflection response.	17
Figure 8 . OFSMC controlled hub angle and tip deflection.	18
Figure 9 . Two-link flexible robot.	19
Figure 10 . Joint 1 controlled response.	20
Figure 11 . Joint 2 controlled response.	20
Figure 12 . Controlled elbow response.	21
Figure 13 . Controlled tip response.	21
Figure 14 . Block diagram of FDI architecture.	23
Figure 15 . Encoder and Filter Simulation Results	25
Figure 16 . Filtered Simulation Residuals and Error Flags	27
Figure 17 . 4-DOF testbed during construction and after completion	29

Tables

Table 1. Optimization Results	30
Table 2. Physical parameters of two mass system.....	30
Table 3. Controller of the two mass system.	30

Table 4.	Physical parameters for the beam.	31
Table 5.	Optimal controller parameters for the beam.	31
Table 6.	Physical parameters for the flexible two-link robot.	31
Table 7.	Optimal controller parameters for the OFSMC design.	32

Intentionally Left Blank

Self-Repairing Control for Damaged Robotic Manipulators

Introduction

Remote operation of a robotic system is a requirement for use in hazardous workplaces and in contaminated cleanup sites. Robust methods of control are needed that can deal with unexpected changes or damage to the system. The goal of this project is to develop methodologies and software to enable damaged robotic manipulators to reconfigure their control systems autonomously, approximating their original for application in hazardous and constrained workspaces. This effort seeks to develop offline techniques for redundant sensor placement and on-line algorithms for utilizing surviving assets. A nonlinear estimation based fault detection and isolation scheme is employed and evaluated using simulated failed sensors.

Optimal Design

The best approach to fault tolerant robotic operation, is to design the robot with this attribute. In this section a method for optimally choosing link lengths, and the nominal operating configuration of a kinematically redundant, planar robot is described. The robot's workspace is maximized for all possible single joint actuator failures. This techniques has the following features:

- Forward kinematics are used, and it is therefore faster than inverse kinematic based schemes.
- There exist parameters for "tuning" the shape of the workspace, but nominally, they may all be set to unity.
- It is directly extendable to multiple joint failures and three-dimensional robots

Problem Description

Joint angles corresponding to a specified end effector position of a kinematically redundant manipulator, in general, are not unique. Furthermore, if link lengths are free design variables, there exist an infinite number of combinations of joint angles and link lengths to achieve a specified end effector location. The problem addressed here is that of designing a kinematically redundant robot. Nominal operation is specified in some region of the hub location. Link lengths and nominal joint angles are to be found resulting in an optimal workspace under any single joint failure condition.

The solution to the optimal sign problem relies on the singular values of the manipulator Jacobian. Therefore, a short discussion is presented regarding the manipulator Jacobian and the meaning of it's singular values.

The manipulator Jacobian is the configuration dependent mapping of joint speeds to end effector velocities.

$$\dot{\underline{x}} = J(\underline{\theta})\dot{\underline{\theta}} \quad \text{EQ(1)}$$

where \underline{x} is the end effector position, J is the manipulator Jacobian, and $\underline{\theta}$ is the evocator of joint angles. Note, that the manipulator Jacobian may be singular for certain joint configurations. The physical meaning of Jacobian singularity is that specific joint speeds are not possible, and correspondingly, certain end effector velocities are not possible. This restricts end effector motion including direction and speed.

The singular values of the manipulator Jacobian may be interpreted in several ways. One interpretation indicates the degree of singularity of the Jacobian. Specifically, small singular values indicate a closeness to singularity. From the previous discussion regarding Jacobian singularity, we can now say that small singular values correspond to end effector motion restriction. A second interpretation requires a brief look back at the Jacobian itself. The Jacobian maps a hypersphere of joint speed to a hyperellipsoid of end effector velocity. The singular values of the Jacobian represent the lengths of the semiaxes of the hyperellipsoid. Once again, small singular values correspond to restricted end effector velocities.

Solution Approach

The design problem was solved using the RQP numerical optimization code in conjunction with the redundant manipulator Jacobian. Specifically:

Given:

- Nominal operation location relative to the hub described by θ_n and r_n the relative angle and radius respectively
- The sum of all link lengths $\sum_i l_i$

Find:

- The nominal joint angles, and link length

Subject to:

- Equality Constraints: θ_n , r_n , and $\sum_i l_i$
- Inequality Constraints: $l_i > 0$

Minimizing:

$$J = \frac{\sum_i w_i \sigma_i}{\sqrt{\sum_i l_i^2}} + w_d \sum_i d_i$$

Where σ_i is the minimum singular value of the i th sub-Jacobian. The i th sub-Jacobian is found by locking the i th joint to the nominal position. Sub-Jacobian weights are given by the w_i . The l_i are

the lengths of the links, while the d_i are the radii of the workspace “holes” resulting from uneven link lengths. For a planar 3 length robot, the “hole” radii can be found as

$$d_1 = (l_2 - l_3)^2$$

$$d_2 = [l_1 - \{(l_2 \cos[\theta_1 + \theta_2] + l_3 \cos[\theta_1 + \theta_2 + \theta_3])^2 + (l_2 \sin[\theta_1 + \theta_2] + l_3 \sin[\theta_1 + \theta_2 + \theta_3])^2\}^{1/2}]^2$$

$$d_3 = [l_3 - \{(l_1 \cos\theta_1 + l_2 \cos[\theta_1 + \theta_2])^2 + (l_1 \sin\theta_1 + l_2 \sin[\theta_1 + \theta_2])^2\}^{1/2}]^2$$

EQ(2)

A weighting term of w_d may be placed on the “holes” term. The physical interpretation of the cost function is to maximize the range of motion from the nominal (first term) while making the workspace “holes” small.

Example

This method was examined for a three-link planar robot with nominal operation location at 45° and a distance 2.0 units from the origin. The total length of the links was fixed to 2.4 units.

Two solutions were obtained. The first solution was for all weights set to unity with the exception of w_d which was set to zero. The second case incorporated the workspace “hole” minimization by setting w_d to unity. The values of the optimal joint configuration θ_i and the optimal link lengths l_i are given in Table 1. Workspace plots for both cases, including failed joint actuators are shown in Figure 1 and Figure 2.

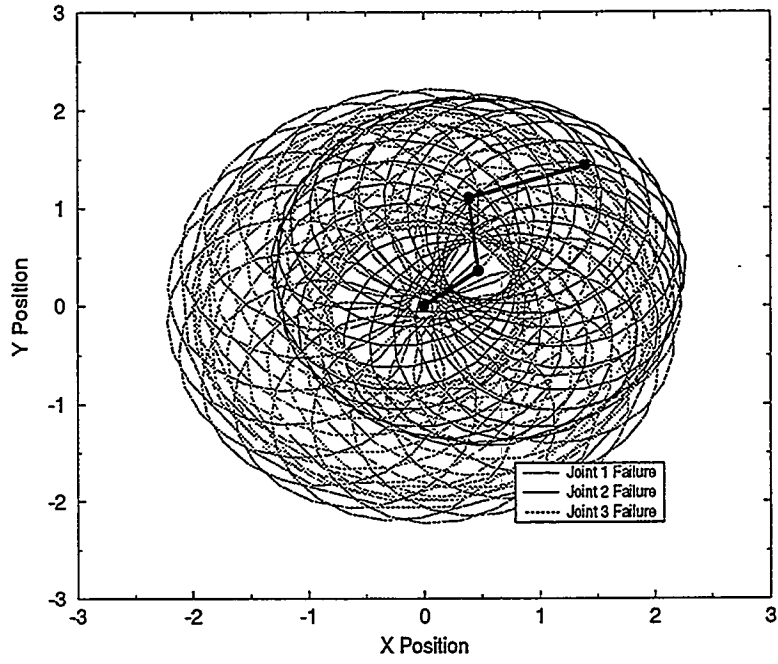


Figure 1. Case 1, No workspace “hole” minimization

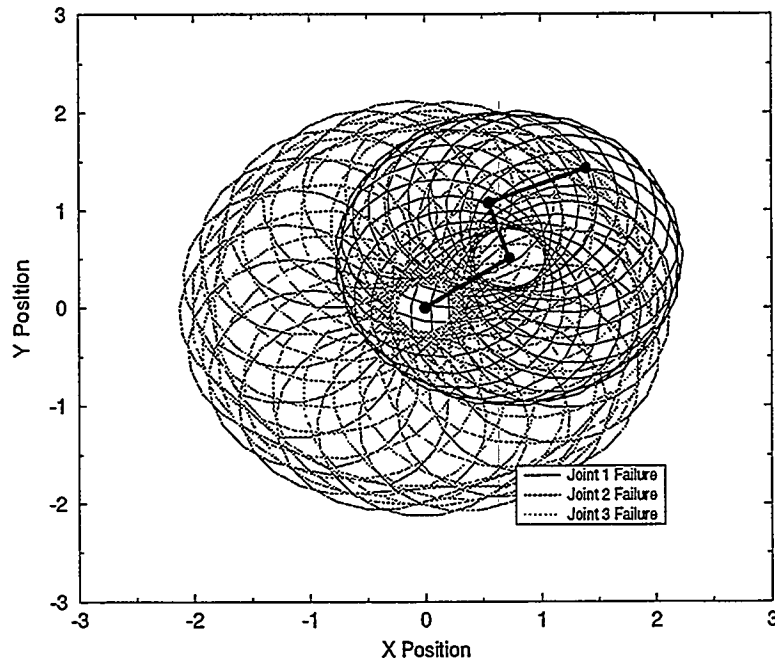


Figure 2. Case 2, With workspace “hole” minimization.

Nonlinear Control

To continue control of a robot with a failed component, the controller should be adaptive with respect to the sensor information used. Furthermore, due to the inherent nonlinearities of direct-drive and hydraulic robots, the controller should accommodate nonlinear systems. For this project a nonlinear control strategy was developed which naturally utilizes available sensor information to generate the torque commands for the joints.

In this section, an output feedback sliding mode control approach is presented for nonlinear systems in general, with application to flexible link robots. Asymptotically stable sliding surfaces are specified in the output space. Equivalent control is implemented via the typical model cancellation approach of sliding mode control. Stability is maintained when the error between state dependent terms of the model and output approximations of those terms is bounded. Application to robotic systems is complicated by the state dependence of the mass matrix. The implications of this are discussed from both a theoretical and a practical perspective. Three design examples are given. The first is a simple nonlinear, two degree-of-freedom spring-mass-damper system intended to illustrate fundamental aspects of the technique. The second is the slewing and vibration control of a single flexible link. The third example is a direct-drive, two-link, flexible robot where angle tracking and vibration suppression are desired.

Output Feedback Sliding Mode Control

Systems describable by equations of the form

$$\begin{aligned} \dot{x} &= N(x, \dot{x}) + B(x)U \\ y &= Cx \end{aligned} \tag{EQ(3)}$$

are considered, where x is an $n \times 1$ vector of degrees-of-freedom, $N(x, \dot{x})$ is an $n \times 1$ vector of nonlinear functions of the x and \dot{x} , $B(x)$ is an $n \times m$ matrix of control weighting coefficients, which in general may be functions of x , U is an $m \times 1$ vector of system inputs, y is an $r \times 1$ vector of measurable outputs, C is an $r \times n$ matrix relating state variables to measurable outputs. As mentioned in the introduction, the sliding surfaces are designed in the output space, implying that sensor output regulation or tracking will yield the desired system motion. The sliding surface may be chosen as

$$s = W(y - y_r) + (\dot{y} - \dot{y}_r) = 0 \tag{EQ(4)}$$

where y_r is the desired sensor output time history and W is a positive definite matrix with real valued elements.

The equivalent control is found by enforcing a condition of stationarity on the sliding surface,

$$\dot{s} = W(\dot{y} - \dot{y}_r) + (\ddot{y} - \ddot{y}_r) = 0 \tag{EQ(5)}$$

and substituting Eq. 3 into Eq. 5

$$CB(x)U = -CN(x, \dot{x}) + \ddot{y}_r - W(\dot{y} - \dot{y}_r) \tag{EQ(6)}$$

The control weighting matrix, $B(x)$ and the vector of nonlinear terms, $N(x, \dot{x})$ are approximated by $B(\hat{x})$ and $N(\hat{x}, \dot{\hat{x}})$ respectively, where

$$\begin{aligned} \hat{x} &= C^* y \\ C^* &= \begin{cases} C^T(CC^T)^{-1} & n > r \\ C^{-1} & n = r \\ (C^TC)^{-1}C^T & n < r \end{cases} \end{aligned} \quad \text{EQ(7)}$$

Eq. 6 may now be written as

$$CB(\hat{x})\underline{U} = -CN(\hat{x}, \dot{\hat{x}}) + \underline{\ddot{y}}_r - W(\underline{\dot{y}} - \underline{\dot{y}}_r) - A \operatorname{sgn}(\underline{s}) \quad \text{EQ(8)}$$

where A is an $r \times r$ constant matrix. The $A \operatorname{sgn}(\underline{s})$ term is added for driving the output to the stable sliding surface of Eq. 4 resulting in the control, \underline{U}

$$\underline{U} = [CB(\hat{x})]^{-1}[-CN(\hat{x}, \dot{\hat{x}}) + \underline{\ddot{y}}_r - W(\underline{\dot{y}} - \underline{\dot{y}}_r) - A \operatorname{sgn}(\underline{s})] \quad \text{EQ(9)}$$

Stability is examined using Lyapunov's direct method with a candidate Lyapunov function as

$$V = \frac{1}{2} \underline{s}^T \underline{s} \quad \text{EQ(10)}$$

The requirement for stability is

$$\begin{aligned} \underline{s}^T \left\{ W(\underline{\dot{y}} - \underline{\dot{y}}_r) + CN(x, \dot{x}) - \underline{\ddot{y}}_r - CB(x)[CB(\hat{x})]^{-1}CN(\hat{x}, \dot{\hat{x}}) + \right. \\ \left. CB(x)[CB(\hat{x})]^{-1}\underline{\ddot{y}}_r - CB(x)[CB(\hat{x})]^{-1}W(\underline{\dot{y}} - \underline{\dot{y}}_r) - \right. \\ \left. CB(x)[CB(\hat{x})]^{-1}A \operatorname{sgn}(\underline{s}) \right\} < 0 \end{aligned} \quad \text{EQ(11)}$$

Establishing stability of the closed-loop system, based on Eq. 11, when the input weighting matrix is a function of all the degrees-of-freedom is a formidable task. Fortunately, many real systems have special forms of $B(x)$ which do facilitate a proof of stability. To this end the input weighting matrix is written as a combination of three matrices

$$B(x) = B_o + B_y(y) + B_{res}(x) \quad \text{EQ(12)}$$

where B_o is a constant matrix, $B_y(y)$ is a matrix whose elements are only a function of the measurable outputs y , and $B_{res}(x)$ is a matrix whose elements are only a function of the degrees-of-freedom different from y . Clearly, if $B_{res}(x)$ is zero or negligible, then there is no approximation in $B(\hat{x})$ and Eq. 11 simplifies to

$$\underline{s}^T [-A \operatorname{sgn}(\underline{s}) + C\{N(x, \dot{x}) - N(\hat{x}, \dot{\hat{x}})\}] < 0 \quad \text{EQ(13)}$$

which is valid for A diagonal with elements satisfying

$$A_{ii} > |C\{N(\underline{x}, \dot{\underline{x}}) - N(\hat{\underline{x}}, \hat{\dot{\underline{x}}})\}| \quad \text{EQ(14)}$$

Again, the vector $\underline{N}(\underline{x}, \dot{\underline{x}})$ may be composed of a constant part, a \underline{y} only part, and a part dependent only on the degrees-of-freedom different from \underline{y} . Exploiting these relationships, during control law implementation, may result in the trivial stability constraint of A being strictly negative.

Design Examples

Example 1: Position regulation of two masses

This first example is presented merely to illustrate the basic design procedure using a system which exhibits both rigid body and flexible body motions. The system under consideration consists of two masses connected by a nonlinear hardening spring and a linear damper. A force acting on the first mass is the sole input to the system. The system is shown in Figure 3. where z_1 and z_2 are the displacements of the individual masses, m_1 and m_2 . The nonlinear hardening spring obeys the following relationship

$$F_{spring} = K_l(z_1 - z_2) + K_{nl}(z_1 - z_2)^3 \quad \text{EQ(15)}$$

where K_l and K_{nl} are the linear and nonlinear spring constants, respectively. The damping coefficient is denoted by C and the force input to the system by F . The particular values used for this example are given in Table 2.

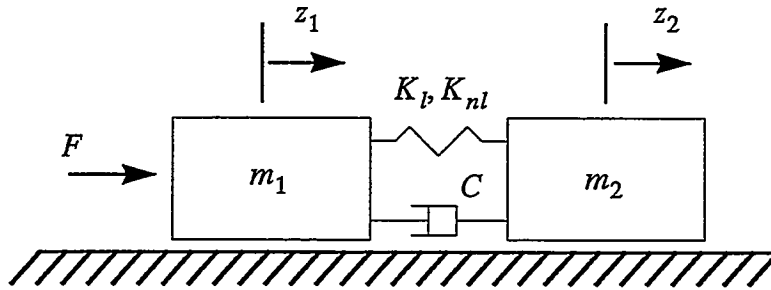


Figure 3. Two mass, nonlinear system.

The control objective is to move the center of mass of the system

$$x_1 = \frac{1}{2}(z_1 + z_2) \quad \text{EQ(16)}$$

to a specified location while suppressing the reciprocating motion of the entire system

$$x_2 = z_1 - z_2 \quad \text{EQ(17)}$$

where the only measurable quantities are the position and velocity of the system center of mass, x_1 and \dot{x}_1 .

The equations of motion, represented using the rigid body and flexible body coordinates x_1 and x_2 may be written in the form of Eq. 3 where

$$\underline{N}(x, \dot{x}) = \begin{bmatrix} -\frac{1}{2} \left(\frac{m_2 - m_1}{m_1 m_2} \right) (K_l x_2 + K_{nl} x_2^3 + C \dot{x}_2) \\ -\frac{1}{2} \left(\frac{m_2 + m_1}{m_1 m_2} \right) (K_l x_2 + K_{nl} x_2^3 + C \dot{x}_2) \end{bmatrix}$$

$$B = \frac{1}{2m_1} \begin{bmatrix} 1 \\ 1 \end{bmatrix} \quad C = [1 \ 0]$$

EQ(18)

The output feedback sliding mode control law is given by Eq. 4 and Eq. 9 with the stability constraint of Eq. 14. Since $n = 2$ and $r = 1$, the vector $\underline{N}(x, \dot{x})$ must be approximated based on the measurable output y and \dot{y} using the pseudo-inverse of Eq. 7 yielding

$$\hat{x} = \begin{bmatrix} 1 \\ 0 \end{bmatrix} y \quad \dot{\hat{x}} = \begin{bmatrix} 1 \\ 0 \end{bmatrix} \dot{y}$$

EQ(19)

In this special case, the term $\underline{N}(x_2, \dot{x}_2)$ is not dependent on the measured quantity, x_1 , therefore, the approximation of $\underline{N}(x_2, \dot{x}_2)$ is exactly zero.

The output feedback sliding mode controller is compared to a simple proportional-derivative (PD) compensator

$$F = K_p(y_r - y) + K_d(\dot{y}_r - \dot{y})$$

EQ(20)

where K_p and K_d are the proportional and derivative error gains respectively. The PD controller gains, and the OFSMC gains, W and A were chosen to limit the peak overshoot to 5.5%. These gains are given in Table 3. Although both control schemes gave similar performance in tracking a reference command, the OFSMC exhibited enhanced disturbance accommodation characteristics. This is shown by the closed-loop performance of the system in response to an initial velocity applied to the second mass. The motion of the system center of gravity, x_1 and the measure of flexible body motion, x_2 are shown in Figure 4 and Figure 5.

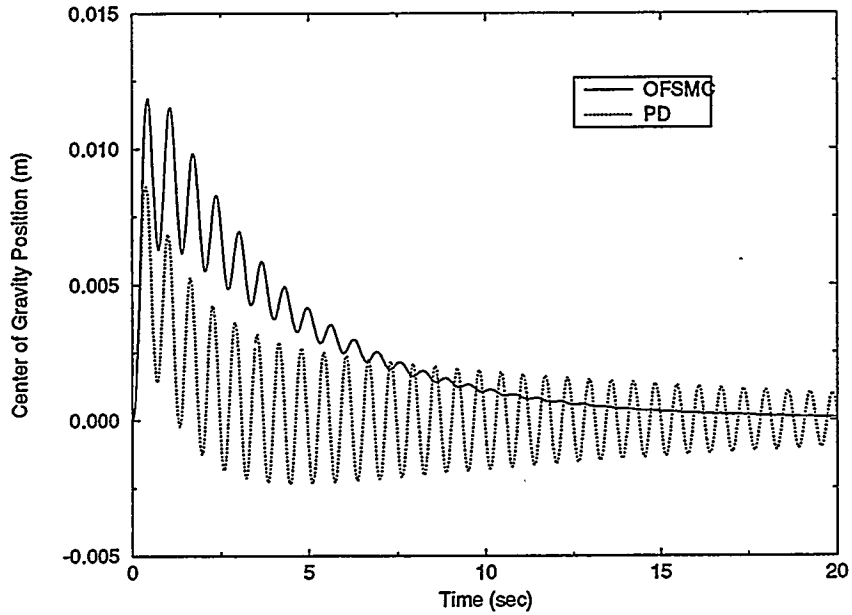


Figure 4. System response of cg.

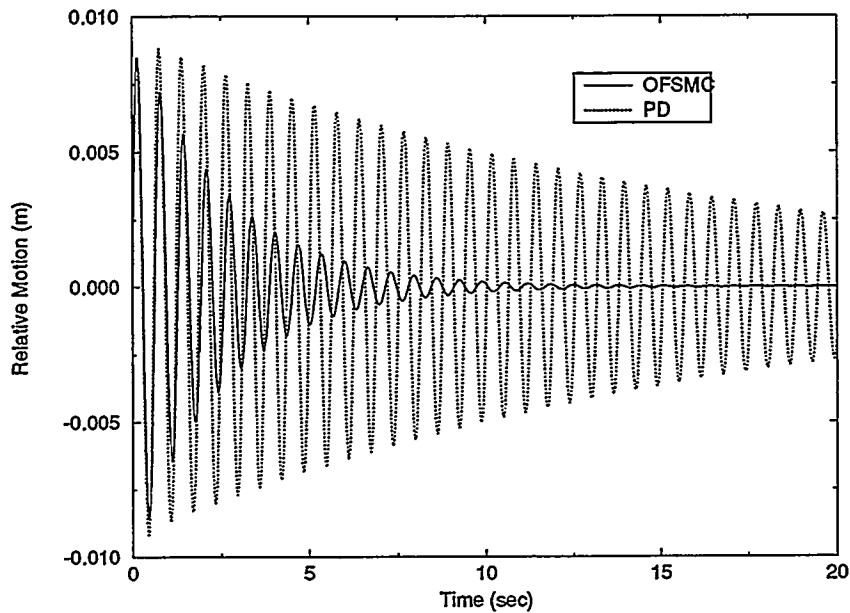


Figure 5. System response of relative motion.

Example 2: Slew angle and vibration control of a flexible beam

This example is intended as a precursor to the flexible two-link robot control problem of Example 3. The system consists of a flexible link attached to a torque actuator. The physical parameters of the link are given in Table 4, and a diagram is shown in Figure 6. The control objective is to slew the hub angle as specified and to damp the induced vibration of the flexible beam.

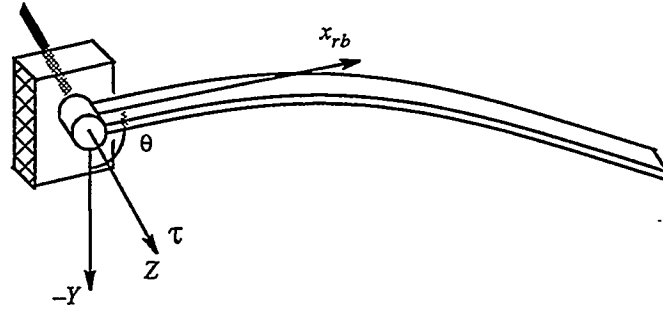


Figure 6. Rotating flexible beam system.

The beam is modeled using the method of quadratic modes (Appendix A) resulting in the equations of motion

$$\begin{aligned}\ddot{\underline{x}} &= -(\mathbf{K}_{lin} + \mathbf{K}_{cent}\dot{\theta}^2)\underline{x} - \mathbf{D}\dot{\underline{x}} + \mathbf{B}\tau \\ y &= \mathbf{C}\underline{x} \\ \underline{x} &= \begin{bmatrix} \theta & q_1 & q_2 & q_3 \end{bmatrix}\end{aligned}\tag{EQ(21)}$$

where \underline{x} is the 4x1 vector of generalized coordinates representing the hub angle, θ , and the flexible body degrees of freedom, q_1 , q_2 and q_3 . The mass normalized stiffness is represented as a linear part, \mathbf{K}_{lin} , and a nonlinear part capturing the centrifugal stiffening, \mathbf{K}_{cent} . Material damping has been assumed at 0.2% and is represented by the matrix \mathbf{D} . The control weighting matrix \mathbf{B} is a constant. The measured output consists of the hub angle and speed, and is reflected by the matrix \mathbf{C} . The derivation of these equations, and the particular numerical values used for this example are detailed in Appendix A. Hub angle response and tip deflection response for a bang-bang hub torque input of magnitude 0.1 N-m is shown in Figure 7. The first mode natural frequency of 4.5 Hz is evident, as is the higher frequency modes of q_2 and q_3 .

The flexible beam model used for the OFSMC control design, is a truncated version of Eq. 21 utilizing only the first mode generalized coordinate, q_1 . The second and third modes were not targeted for control, however, were used in the simulation to examine spillover effects. The truncated version of Eq. 21 is easily written in the form of Eq. 3 to facilitate control design. Instead of using Eq. 7 to form \mathbf{C}^* , the two elements of this vector were left free, and chosen to optimize the performance of the closed-loop system. Since this results in four control parameters, a systematic procedure is employed for tuning the closed-loop controller. Specifically, a numerical optimization code is used to optimally choose the values of A , W and \mathbf{C}^* while minimizing the cost function

$$J = \alpha \int_{t_0}^{t_f} (\theta_{ref} - \theta)^2 dt + \beta \int_{t_0}^{t_f} q_1^2 dt\tag{EQ(22)}$$

where the cost function calculation start time, t_0 is chosen to be the same as the desired maneuver time of 2.0 seconds. The weighting coefficients for the hub angle error, α and the beam residual vibration, β were chosen as unity. The cost function evaluation time, $t_f = 4.0$ seconds, is chosen so as to capture averaged residual errors.

The reference motion of the hub is generated from a spline fit of the initial hub angle of 0 radians to the final hub angle of 1.0 radians. The OFSMC, closed-loop response of this system is shown in Figure 8 along with the reference hub command. The optimized controller parameters are given in Table 5.

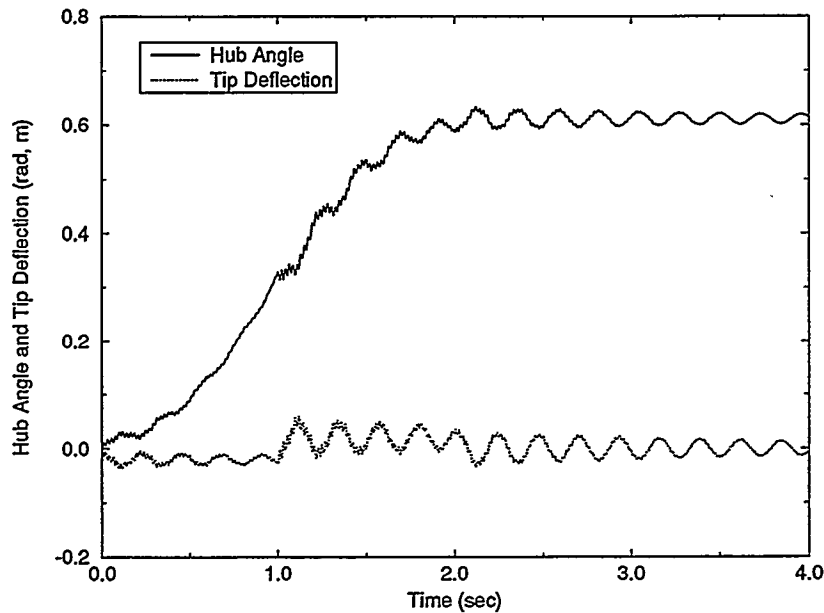


Figure 7. Nominal hub angle and tip deflection response.

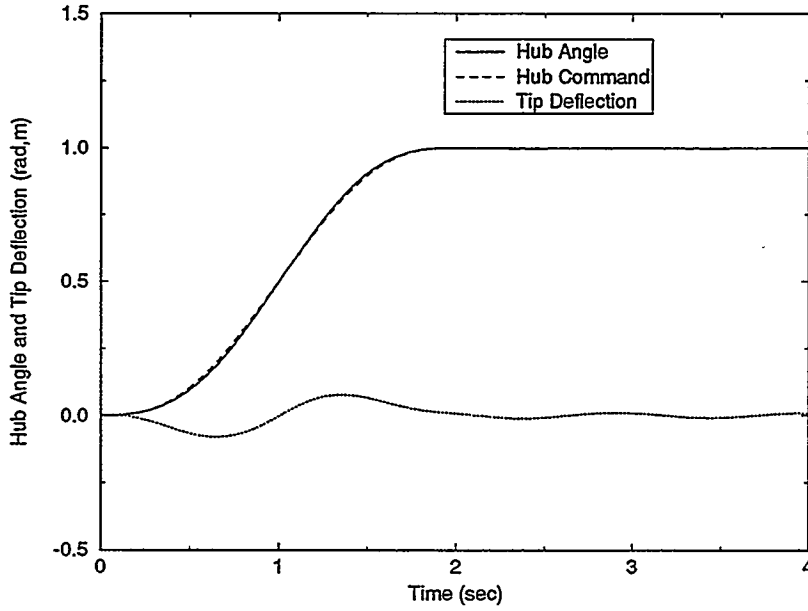


Figure 8. OFSMC controlled hub angle and tip deflection.

Example 3: Flexible two-link robot OFSMC

The system considered consists of two serially connected flexible links, each with its own torque actuator. A diagram is shown in Figure 9, with the physical parameters in Table 6. The OFSMC method of Section 3 is applied to the robot to achieve joint command tracking and link vibration suppression. The maneuver considered is a simultaneous rotation of each joint from 0 to 1 radians where the second joint rotation angle is relative to the first joint angle. Again, the method of quadratic modes is used for system modeling as described in Appendix B. The system outputs are the joint rotational quantities, $\theta_1, \hat{\theta}_1, \theta_2$ and $\hat{\theta}_2$. Flexible body generalized coordinates are denoted as q_1^i for the first link and q_2^j for the second link. The configuration vector, \underline{x} is defined as

$$\underline{x}^T = \left[\theta_1 \ q_1^1 \ \theta_2 \ q_2^1 \right] \quad \text{EQ(23)}$$

Writing the equations of motion in the form of Eq. 3 results in a configuration dependent input weighting matrix, $\mathbf{B}(\underline{x})$. This is primarily due to the inversion of the configuration dependent mass matrix of the robot. Expansion of this matrix, as in Eq. 12, indicates the presence of constant terms, \mathbf{B}_o , terms dependent on the measured quantities, $\mathbf{B}_y(\underline{y})$, and terms due to the unmeasured flexible body generalized coordinates, $\mathbf{B}_{res}(\underline{x})$. Fortunately, the $\mathbf{B}_{res}(\underline{x})$ is small in magnitude compared to the other two, and is negligible. The stability constraint of Eq. 14 is therefore appropriate.

The first mode of each link is targeted during controller design. The equations of motion in Appendix B are readily cast in the form of Eq. 3. Unlike the previous two examples, the scalar controller parameter, W and A are 2x2 matrices whereas C^* is 4x2. The numerical optimization procedure, used in example 2, is employed for choosing control parameters where the cost function minimized is

$$J = \sum_{i=1}^2 \int_{t_0}^{t_f} (q_i^1)^2 dt \quad \text{EQ(24)}$$

Unlike Eq. 22, angle errors are not included in the cost function since they are specified as equality constraints. The optimal parameters are given in Table 6 and the closed loop results of the OFSMC of Eq. 9 are shown in Figure 10 through Figure 13.

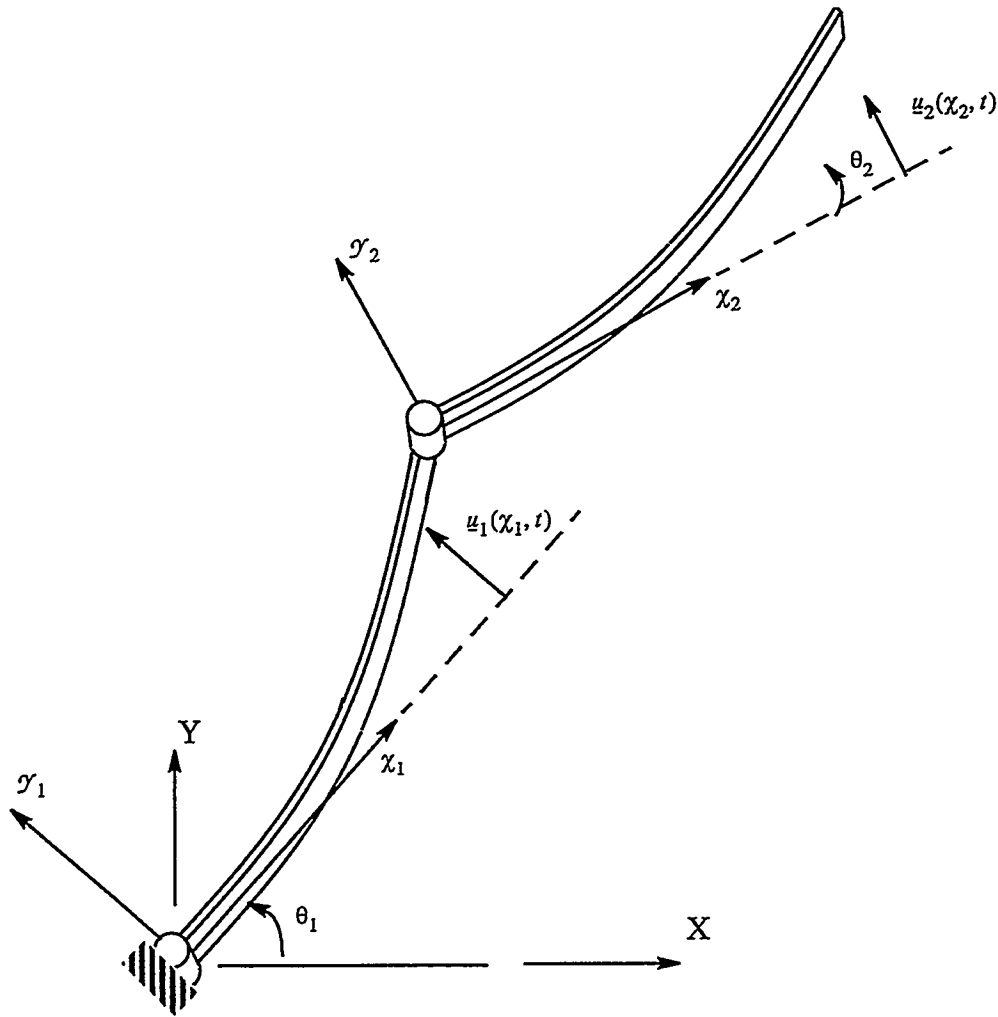


Figure 9. Two-link flexible robot.

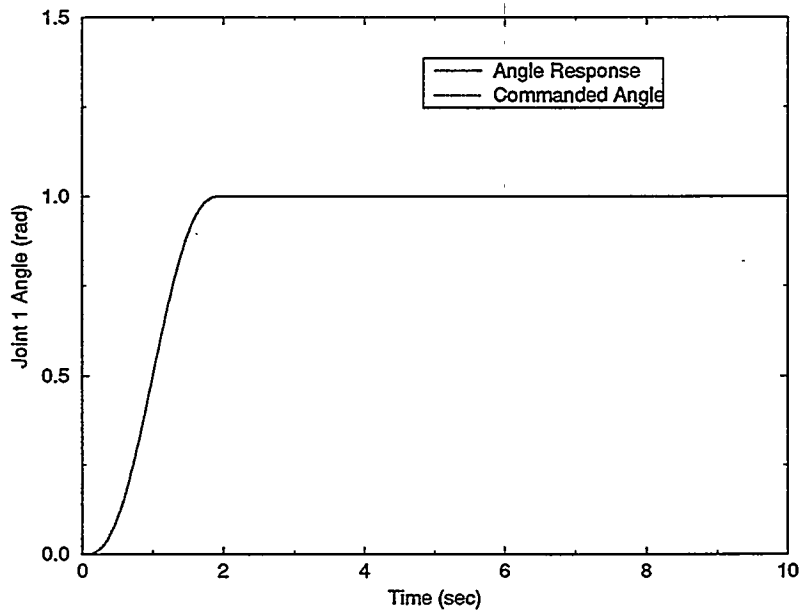


Figure 10. Joint 1 controlled response.

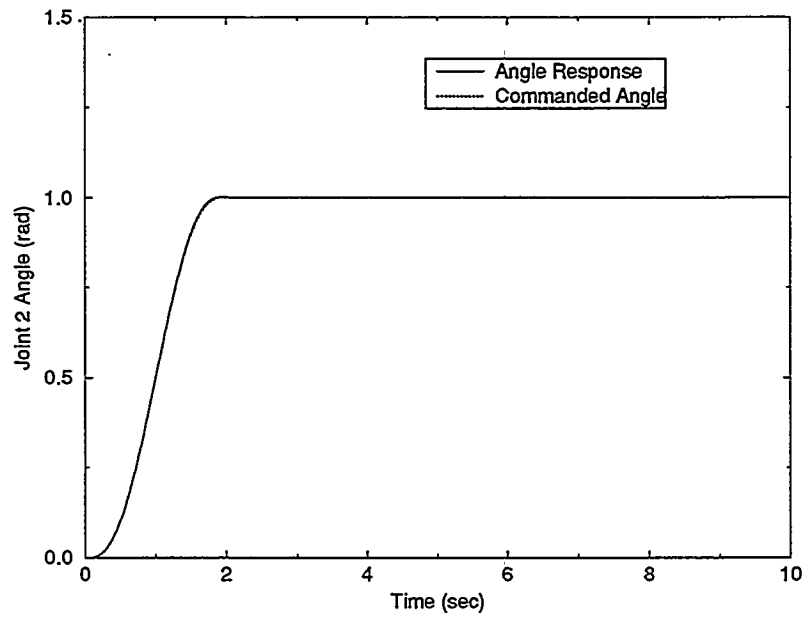


Figure 11. Joint 2 controlled response.

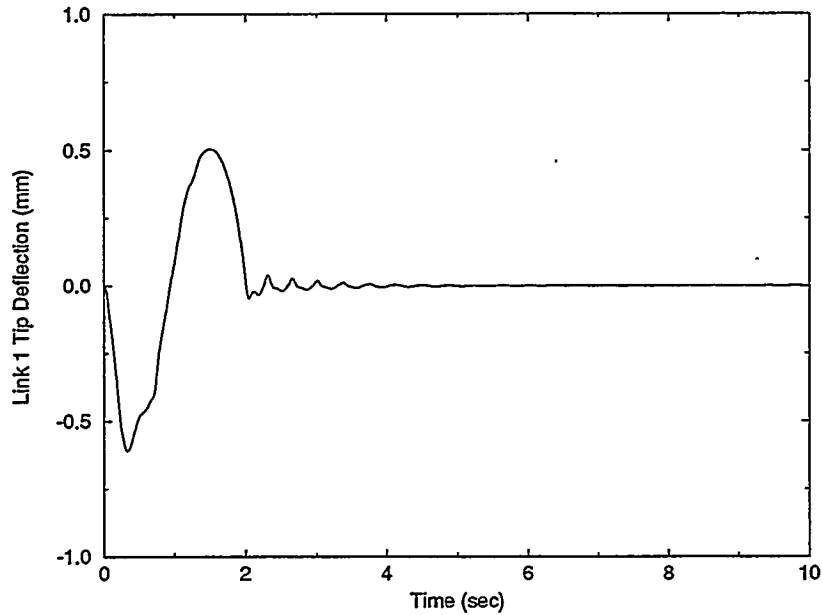


Figure 12. Controlled elbow response.

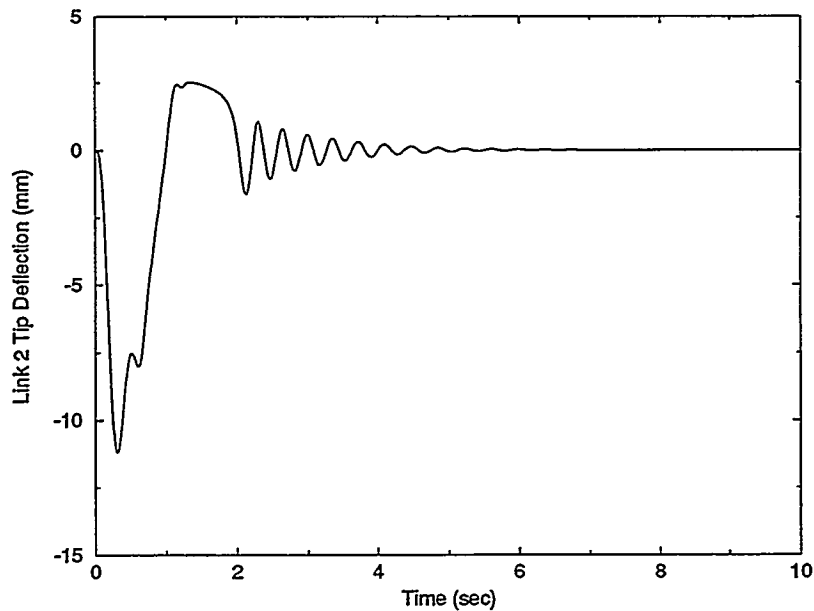


Figure 13. Controlled tip response.

Summary

An output feedback sliding mode control method has been presented for nonlinear systems in general with specific application to flexible link robots. A constraint has been derived, based on Lyapunov's direct method, ensuring stability of the closed-loop system. For systems, including rigid link robots, with equations of motion where the input weighting coefficient matrix is constant, or dependent only on the measured quantities, the stability constraint is directly assessable. For flexible link robots with joint measurements only, or systems with input weighting matrices

dependent on unmeasured states, the stability constraint becomes difficult to evaluate. Fortunately, when this dependence is negligible, as with flexible link robots, the simplified stability constraint is valid.

Path-Planning

Robotic path planning is an important component of an overall fault-tolerant system. Should an actuator fail, the previously planned trajectory becomes invalid. For continued operation, a new path must be devised. Furthermore, if optimal paths are required, then the path planning algorithm must take into account the dynamics of the robot. For this project, two computationally efficient, dynamic path-planner algorithms were developed. The first method is based on dynamic programming [1], while the second method relies on an efficient, quadratic programming-like algorithm [2]. Both methods generate a path solution requiring order(N) calculations, where N is the number of path discretization points. The second method was experimentally verified using the Sandia planar, three-link robot test bed.

Fault-Detection and Isolation

Central to the development of a fault tolerant robot system, is the ability to detect that an anomaly has occurred and to isolate the component. This process is commonly referred to as fault detection and isolation (FDI). Once the failure has been identified, the control system can take appropriate action to mitigate damage and allow the robot to continue operation. An extended Kalman filter approach was developed, based on the closed-loop dynamic model for all possible failed scenarios, for FDI.

The FDI strategy is based on the identification of n failure modes of the system. The closed-loop model (typically nonlinear) of the robot for each of the n failure modes is used in conjunction with an extended Kalman Filter to estimate the actual joints states of the robot. These joint states are then compared to the sensor data. When the valid sensor joint data coalesce with the valid joint state for any of the estimated states, then the fault has been simultaneously detected and identified. The nominal robot joint states are also estimated, using a linear Kalman Filter, as an additional check for simply detected that a fault has occurred.

Once the fault has been identified, the robot joint sensor data, used for the joint servo controllers, is modified by replacing the invalid sensor data with the estimated signal from the appropriate extended Kalman Filter. A block diagram of this system is shown in Figure 14.

This architecture was simulated for a two-link robot, and the results for a failure of a joint #2 tachometer failure shown in Figure 15 through Figure 16. The maneuver slews both links to +23 degrees from an initial 0-degree (both links aligned) orientation. An encoder to measure joint angles and a tachometer to measure joint angle rates were simulated at each joint. The control system employs a computed-torque scheme to cancel the nonlinear dynamics and proportional-derivative control on the remaining 2nd-order linear dynamics to attain the desired angles. During

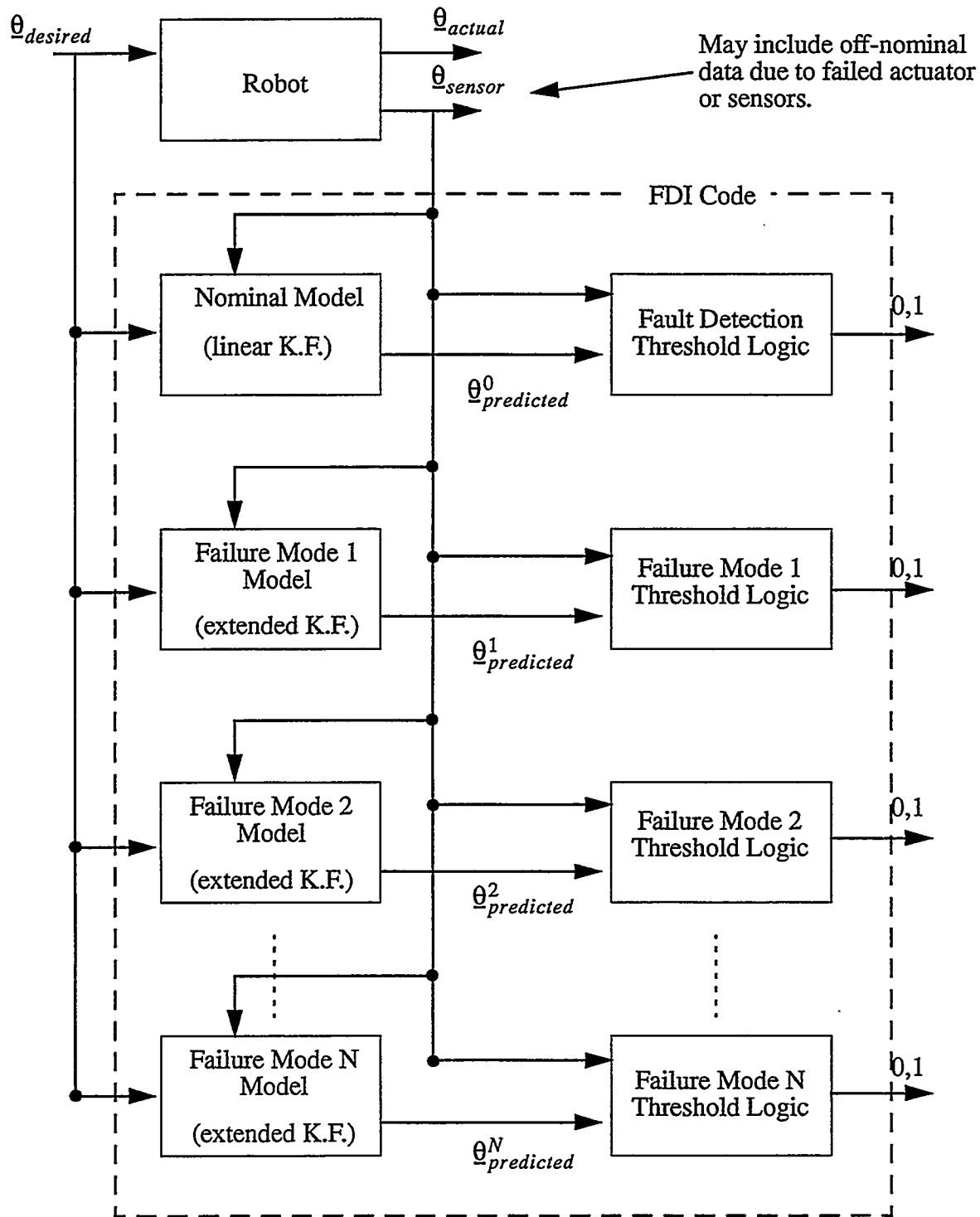


Figure 14. Block diagram of FDI architecture.

the maneuver, the joint 2 tachometer will be “synthetically” failed and estimated rate values will be used in its place.

The Kalman Filter equations are as follows:

$$\text{State Propagation : } x_p(t_k) = x_u(t_{k-1}) + \int_{t_{k-1}}^{t_k} f(x_u(\tau), u(\tau), \tau) d\tau$$

$$\text{Covariance Propagation : } P_p(t_k) = P_u(t_{k-1}) + \int_{t_{k-1}}^{t_k} [F(\tau)P_u(\tau) + P_u(\tau)F^T(\tau) + Q(\tau)] d\tau$$

$$\text{Filter Gain : } K(t_k) = P_p(t_k)H^T(t_k)[H(t_k)P_p(t_k)H^T(t_k) + R(t_k)]^{-1}$$

$$\text{State Estimate Update : } x_u(t_k) = x_p(t_k) + K(t_k)[z(t_k) - h(x_p(t_k), t_k)]$$

$$\text{Covariance Update : } P_u(t_k) = [I - K(t_k)(H(t_k))]P_p(t_k)$$

where the p and u subscripts denote propagation and update at sample times, t_k , x is the vector of dynamical states, f represents the nonlinear dynamics model, u is the vector of controls, P is the covariance matrix of the linearized states, F is the linearized dynamics matrix, Q is the matrix of linearized state propagation noise covariances, H is the linearized sensor model, R is the matrix of sensor noise covariances, h is the nonlinear sensor model, and I is the identity matrix.

After some experimentation, it was decided that the Kalman filter residuals, $z(t_k) - h(x_p(t_k), t_k)$, would provide the necessary information to determine if a fault had occurred. If no failure had occurred the Kalman filter modeling the nominal “healthy” dynamics would soon converge and the residuals would approach zero. However, if a failure had occurred then the filter would be using an incomplete set of measurements (as well as dynamics) and would generate erroneous state estimates and divergent residual behavior.

The tachometer residuals were still noisy after Kalman filtering and all residuals were then Butterworth-filtered with a low-pass, 60-Hz cutoff frequency configuration assuming a sample rate of 500 Hz. This provided graphic visual evidence of the fault as shown in Figure 15. However for the system to act autonomously, a mathematical determination of “fault” had to be made. This was done by “windowing” every 21 data points and integrating the area under the individual residual curves (using Simpson’s method) and dividing by the time length of the window. When this exceeded a preset threshold, a flag (equal to a value of 1.0) was “thrown” (as seen in Figure 16).

In the example shown, the fault was preset to occur at 1.5 seconds. Note that the error was “flagged” almost instantaneously. Note also that false flags occur before the Kalman filter has converged to the true unfailed condition. This will have to be accounted for under actual operating conditions.

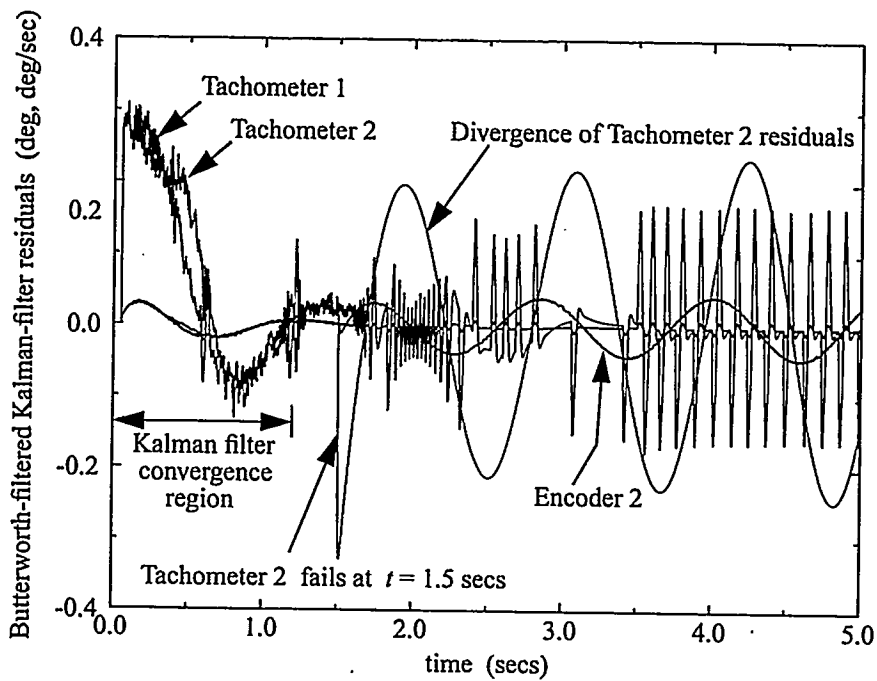
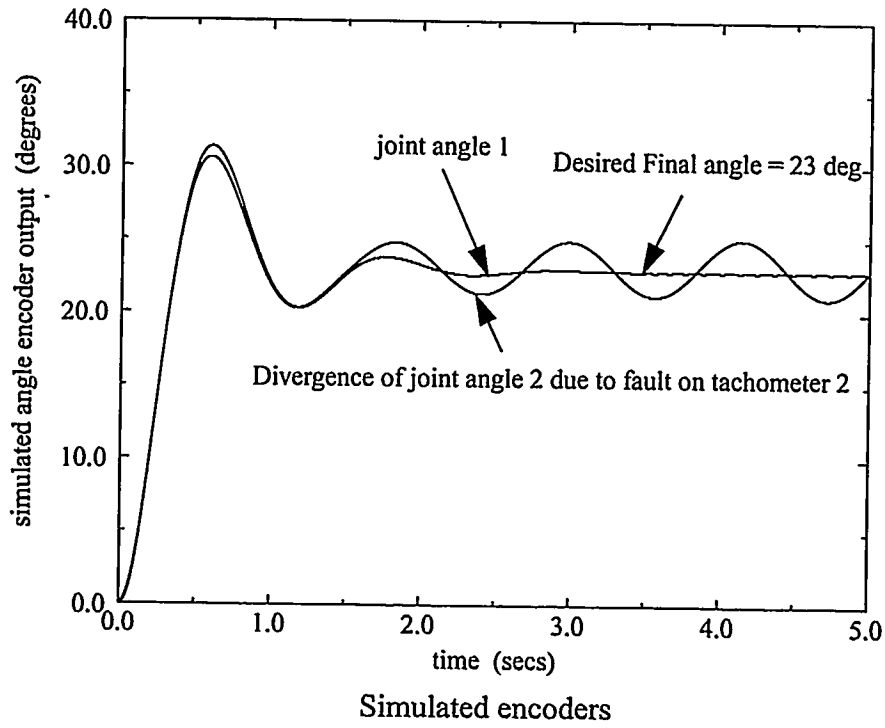
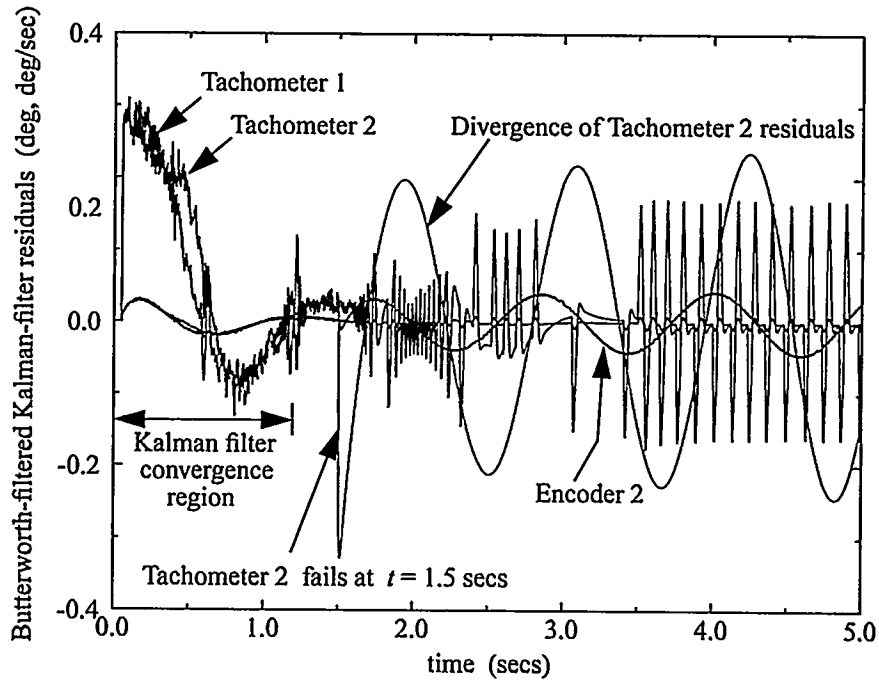
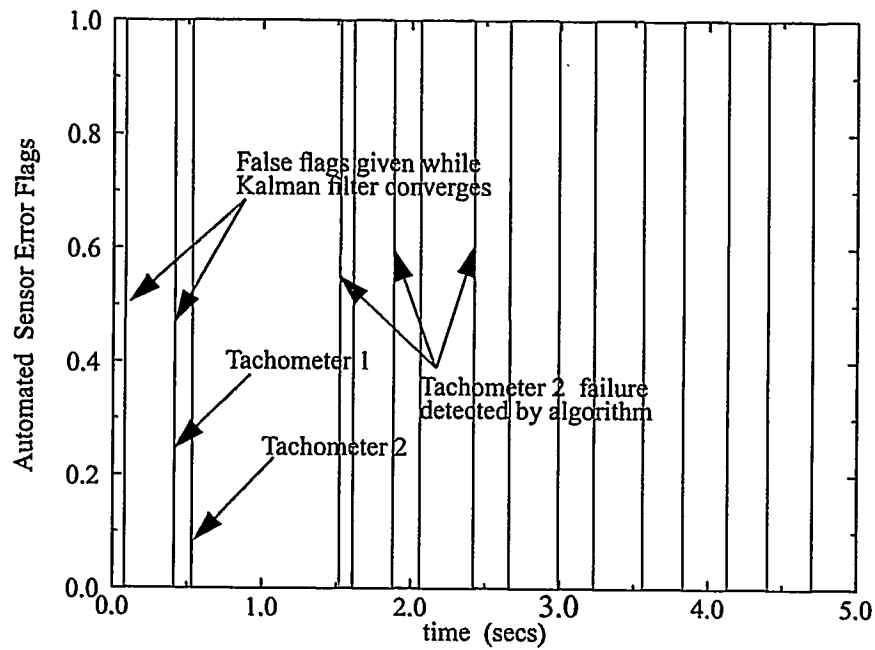


Figure 15. Encoder and Filter Simulation Results

Intentionally Left Blank



Simulated Kalman and Butterworth-filtered sensor residuals



Simulated Error Flags

Figure 16. Filtered Simulation Residuals and Error Flags

Intentionally Left Blank

Test-Bed

Some degree of fault-tolerance can be accommodated via software using FDI approaches and adaptive control. However, the most effective fault-tolerance is realized by hardware redundancy. Unfortunately, this is usually at the expense of weight and system complexity. As part of this project, joint actuator redundancy was addressed through the development of a hydraulic, 2-axis joint design. As a proof of concept, a 4 degree-of-freedom (DOF) testbed was developed incorporating this design. The 4 DOF test bed, shown in Figure 17 , incorporates two hydraulic, two-axis joints where each DOF torque actuator capable of 2100 N-m.

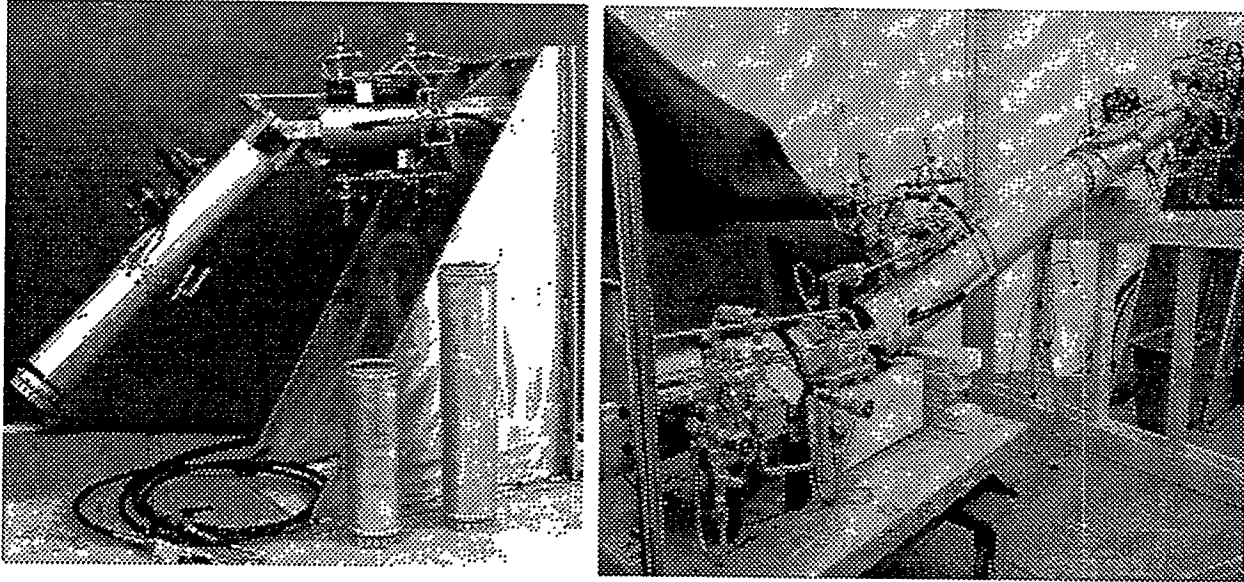


Figure 17. 4-DOF testbed during construction and after completion

References

- [1] C. R. Dohrmann and R.D. Robinett, "Robot Trajectory Planning via Dynamic Programming," Proceedings of the Fifth International Symposium on Robotics and Manufacturing: Research, Education, and Applications, pp. 75-81, 1994.
- [2] B. J. Driessen, "Efficient Numerical Methods for Obtaining and Tracking Minimum Time Trajectories of Dynamic Systems" Ph.D. Dissertation, Georgia Tech University, 1996.

Tables

Case #	θ_1 (deg)	θ_2 (deg)	θ_3 (deg)	l_1	l_2	l_3
1	34.9	72.2	-84.2	0.89	0.60	0.91
2	37.5	58.9	-78.2	0.60	0.75	1.06

Table 1. Optimization Results

Symbol	Units	Value
m_1	kg	1.0
m_2	kg	0.1
C	kg/s	0.2
K_l	kg/s/s	8.0
K_{nl}	kg/(m*m*s*s)	50.0

Table 2. Physical parameters of two mass system.

Symbol	Units	Value
A	1/sec	0.4
W	1/sec	1.9
K_p	kg/s/s	5.0
K_d	kg/s	7.0

Table 3. Controller of the two mass system.

Symbol	Description	Units	Value
ρ	Density	kg/m/m/m	2700
E	Young's Modulus	GPa	70
L	Length	m	1
w	Width	mm	76.2
h	Thickness	mm	1.6

Table 4. Physical parameters for the beam.

Symbol	Units	Value
W	1/sec	100.07
A	1/sec	100.04
C_1^*	n.d.	0.694
C_2^*	n.d.	-0.00651

Table 5. Optimal controller parameters for the beam.

Symbol	Description	Units	Value
ρ_1	Density: Link 1	kg/m/m/m	2700
ρ_2	Density: Link 2	kg/m/m/m	2700
E_1	Young's Modulus: Link 1	GPa	70
E_2	Young's Modulus: Link 2	GPa	70
L_1	Length: Link 1	m	0.463
L_2	Length: Link 2	m	0.489
w_1	Width: Link 1	mm	152
w_2	Width: Link 2	mm	76.2
h_1	Thickness: Link 1	mm	4.76
h_2	Thickness: Link 2	mm	1.59

Table 6. Physical parameters for the flexible two-link robot.

Symbol	Units	Value
W_{11}	1/sec	10.0
W_{22}	1/sec	10.0
A_{11}	1/sec	10.0
A_{22}	1/sec	10.0
C_{11}^*	1/sec	1.153
C_{12}^*	n.d.	2.83E-06
C_{13}^*	n.d.	0.0
C_{14}^*	n.d.	0.0
C_{21}^*	n.d.	0.0
C_{22}^*	n.d.	0.0
C_{23}^*	n.d.	1.105
C_{24}^*	n.d.	1.06E-04

Table 7. Optimal controller parameters for the OFSMC design.

Appendix A

Appendix A describes the modeling of the slewing flexible link system of Example 1. Analytic expressions for the equations of motion along with the actual numerical values are given. Appendix B presents a similar description of the governing equations for the two-link flexible robot of Example 2.

Appendix A

The slewing flexible beam, shown in Figure 6, is modeled using the method of quadratic modes. This assumed modes method employs an expansion of the deformation $\underline{u}(\chi, t)$ as

$$\underline{u}(\chi, t) = q^i(t)\underline{\phi}^i(\chi) + q^j(t)q^j(t)g^{ij}(\chi) \quad (\text{A-1})$$

where the mode shapes $\underline{\phi}^i$ are the typical cantilevered linear mode shapes for lateral beam vibration. The quadratic modes g^{ij} represent foreshortening of the beam consistent with the linear mode shapes. The quadratic mode shapes for a beam are given by

$$\frac{\partial}{\partial \chi^2} g^{ij} = -\frac{1}{2} \frac{\partial}{\partial \chi^2} \phi^i \frac{\partial}{\partial \chi^2} \phi^j \quad (\text{A-2})$$

The deformation generalized coordinates are represented by the $q^i(t)$ terms.

The equation of motion for both the rigid body, θ and the flexible body, q^i degrees of freedom are found using the Lagrange's equations. To this end, the kinetic energy, T , the potential energy, V , and the work from external forces, W_F are used to form the Lagrangian, $L = T - V + W_F$. The kinetic energy is

$$T = \frac{1}{2} \int_0^L m_o [\dot{\theta}^2 (q^i q^j \phi^i \phi^j + 2\chi q^i q^j g^{ij} + \chi^2) + \dot{q}^i \dot{q}^j \phi^i \phi^j + 2\dot{\theta} \dot{q}^i \chi \phi^i] d\chi \quad (\text{A-3})$$

where m_o is the mass per unit length of the beam. The potential energy is

$$V = \frac{1}{2} EI q^i q^j \int_0^L \phi^{i''} \phi^{j''} d\chi \quad (\text{A-4})$$

where I is the mass moment of inertia of the beam. The work from external forces is

$$W_F = \tau q^i \int_0^L \phi^i \eta d\chi + \tau \theta \quad (\text{A-5})$$

The Euler-Lagrange equation for the rigid body motion is

$$\frac{d}{dt}\left(\frac{\partial L}{\partial \dot{\theta}}\right) - \frac{\partial L}{\partial \theta} = 0 \quad (\text{A-6})$$

resulting in the equation of motion

$$\frac{1}{3}L^3 m_o \ddot{\theta} + \left(m_o \int_0^L \chi \phi^i d\chi \right) \ddot{q}^i = \tau \quad (\text{A-7})$$

The Euler-Lagrange equations for the flexible body degrees of freedom are

$$\frac{d}{dt}\left(\frac{\partial L}{\partial \dot{q}^i}\right) - \frac{\partial L}{\partial q^i} = 0 \quad (\text{A-8})$$

resulting in flexible body equations of motion

$$\begin{aligned} & m_o \ddot{\theta} \int_0^L \chi \phi^i d\chi + m_o \ddot{q}^j \int_0^L \phi^i \phi^j d\chi + \\ & \left[EI \int_0^L \phi^{i''} \phi^{j''} d\chi - \dot{\theta}^2 m_o \int_0^L (\phi^i \phi^j + 2\chi g^{ij}) d\chi \right] q^j = -\tau \phi^{i'}(0) \end{aligned} \quad (\text{A-9})$$

Using cantilevered mode shapes of the form

$$\begin{aligned} \phi^i = A^i [& (\sin \beta^i L - \sinh \beta^i L)(\sin \beta^i \chi - \sinh \beta^i \chi) - \\ & (\cos \beta^i L + \cosh \beta^i L)(\cos \beta^i \chi - \cosh \beta^i \chi)] \end{aligned} \quad (\text{A-10})$$

where the $\beta^i L = 1.875, 4.694, 7.855$ for mode shapes 1 through 3. The normalization coefficients, A^i are chosen so as to mass normalize the term

$$m_o \int_0^L \phi^i \phi^j d\chi \quad (\text{A-11})$$

Using the values of Table 4, numerical expressions for the equations of motion may be written as in Eq. 21

$$K_{lin} = \begin{bmatrix} 0 & 26507.5 & 165886.7 & 465452.9 \\ 0 & 26466.4 & 165383.4 & 464041.0 \\ 0 & 4222.9 & 27970.6 & 74150.5 \\ 0 & 1505.0 & 9418.6 & 38528.2 \end{bmatrix} \quad (\text{A-12})$$

$$K_{cent} = \begin{bmatrix} 0 & 26.1 & 133.3 & 131.9 \\ 0 & 26.2 & 132.2 & 130.7 \\ 0 & 3.5 & 26.7 & 21.2 \\ 0 & 0.7 & 7.7 & 24.3 \end{bmatrix} \quad (\text{A-13})$$

$$D = \begin{bmatrix} 0 & 0 & 0 & 0 \\ 0 & 0.3 & 0 & 0 \\ 0 & 0 & 1.6 & 0 \\ 0 & 0 & 0 & 4.4 \end{bmatrix} \quad (\text{A-14})$$

$$B = \begin{bmatrix} 4233.8 \\ 4221.0 \\ 674.5 \\ 240.4 \end{bmatrix} \quad (\text{A-15})$$

Intentionally Left Blank

Appendix B

The flexible two-link system is shown in Figure 9 where the joint angle θ_1 is measured between the tangent of the connection of the first link to the hub and the inertial X axis. The deformation of the first link, $u_1(\chi_1, t)$ is measured relative to the rotating X_1 axis. The joint angle θ_2 is measured between the tangent of the connection of the second link to the second joint and the rotating X_1 axis. The deformation of the second link, $u_2(\chi_2, t)$ is measured relative to the rotating X_2 axis. The rotating X_1, Y_1, Z_1 coordinate system is attached to the first link and rotates with speed, $\dot{\theta}_1$. The rotating X_2, Y_2, Z_2 system is attached to the second link and rotates with speed $\dot{\theta}_2$.

Lagrange's equations are applied to the system with Lagrangian

$$L = T - V + W_F \quad (\text{B-1})$$

The kinetic energy, T is

$$T = \frac{1}{2} m_1 \int_0^{L_1} \dot{x}_1^T(\chi_1, t) \dot{x}_1(\chi_1, t) + \frac{1}{2} m_2 \int_0^{L_1} \dot{x}_2^T(\chi_2, t) \dot{x}_2(\chi_2, t) \quad (\text{B-2})$$

where m_1 and m_2 are the mass per unit length of links 1 and 2. The displacement of any particle along the links is denoted by x_1 and x_2 , with reference point, in the undeformed configuration, given by χ_1 and χ_2 are found via a kinematic analysis, using the quadratic modes expansion as

$$\begin{aligned} \dot{x}_1 = & [-\dot{\theta}_1 q_1^i \phi_1^i + 2\dot{q}_1^i q_1^j g_1^{ij}] \hat{i}_1 + \\ & [\chi_1 \dot{\theta}_1 + \dot{q}_1^i \phi_1^i + \dot{\theta}_1 q_1^i q_1^j g_1^{ij}] \hat{j}_1 \end{aligned} \quad (\text{B-3})$$

$$\begin{aligned} \dot{x}_2 = & [-\chi_2(\dot{\theta}_1 + \dot{\theta}_2) s_2 - \dot{\theta}_1 q_1^i \phi_1^i(L_1) - \dot{\theta}_2 q_2^i \phi_2^i c_2 - \dot{q}_2^i \phi_2^i s_2 + \\ & 2\dot{q}_2^i q_2^j g_2^{ij} c_2 + 2\dot{q}_1^i q_1^j g_1^{ij}(L_1) - (\dot{\theta}_1 + \dot{\theta}_2) q_2^i q_2^j g_2^{ij} s_2] \hat{i}_1 + \\ & [L_1 \dot{\theta}_1 + \chi_2(\dot{\theta}_1 + \dot{\theta}_2) c_2 - \dot{\theta}_2 q_2^i \phi_2^i s_2 + \dot{q}_2^i \phi_2^i c_2 + \dot{q}_1^i \phi_1^i(L_1) + \\ & 2\dot{q}_2^i q_2^j g_2^{ij} s_2 + (\dot{\theta}_1 + \dot{\theta}_2) q_2^i q_2^j g_2^{ij} c_2 + \dot{\theta}_1 q_1^i q_1^j g_1^{ij}(L_1)] \hat{j}_1 \end{aligned} \quad (\text{A-16})$$

Applying Lagrange's equations and substituting in the physical parameters of Table 6, the equations of motion may be written in the form

$$M(x) \ddot{x} + N(x, \dot{x}) = B(x) \tau \quad (\text{B-4})$$

where the explicit values of the coefficients of each term are

$$M_{11} = 0.11 + 0.04c_2 - 0.10s_2q_1^1 \quad (\text{B-5})$$

$$M_{21} = -0.26 - 0.05c_2 + 0.08s_2q_1^1 \quad (\text{B-6})$$

$$M_{31} = -0.01 + 0.02c_2 - 0.05s_2q_1^1 \quad (\text{B-7})$$

$$M_{41} = -0.03 - 0.04c_2 + 0.11s_2q_1^1 - 0.83s_2q_2^1 \quad (\text{B-8})$$

$$M_{12} = M_{21} \quad (\text{B-9})$$

$$M_{22} = 0.67 \quad (\text{B-10})$$

$$M_{32} = -0.05c_2 + 0.08s_2q_1^1 - 0.11s_2q_2^1 \quad (\text{B-11})$$

$$M_{42} = 0.11c_2 \quad (\text{B-12})$$

$$M_{13} = M_{31} \quad (\text{B-13})$$

$$M_{23} = M_{32} \quad (\text{B-14})$$

$$M_{33} = 0.01 \quad (\text{B-15})$$

$$M_{43} = -0.03 \quad (\text{B-16})$$

$$\dot{M}_{14} = M_{41} \quad (\text{B-17})$$

$$M_{24} = M_{42} \quad (\text{B-18})$$

$$M_{34} = M_{43} \quad (\text{B-19})$$

$$M_{44} = 0.07 \quad (\text{B-20})$$

$$N_1 = (0.04s_2 + 0.10c_2q_1^1)\dot{\theta}_1\dot{\theta}_2 + (0.02s_2 + 0.05c_2q_1^1 + 0.04c_2q_2^1)\dot{\theta}_2^2 + 0.10s_2\dot{q}_1^1\dot{\theta}_1 - 0.08s_2\dot{q}_2^1\dot{\theta}_2 \quad (\text{B-21})$$

$$N_2 = (-0.10s_2 - 0.25c_2q_1^1 + 0.11c_2q_2^1)\dot{\theta}_1\dot{\theta}_2 - (0.05s_2 + 0.17c_2q_1^1 + 0.12q_1^1)\dot{\theta}_1^2 - (0.05s_2 + 0.08c_2q_1^1 - 0.11c_2q_2^1)\dot{\theta}_2^2 - 0.11\dot{q}_2^1\dot{\theta}_1 + 0.21s_2\dot{q}_2^1\dot{\theta}_2 - 1271q_1^1 \quad (\text{B-22})$$

$$N_3 = (-0.02s_2 - 0.05c_2q_1^1)\dot{\theta}_1^2 + 0.10s_2\dot{q}_1^1\dot{\theta}_1 \quad (\text{B-23})$$

$$N_4 = -0.16q_2^1\dot{\theta}_1\dot{\theta}_2 - (0.83q_2^1c_2 + 0.08q_2^1)\dot{\theta}_1^2 - 0.01q_2^1\dot{\theta}_2^2 - \\ 0.11s_2\dot{q}_1^1\dot{\theta}_1 - 20.2q_2^1 \quad (\text{B-24})$$

$$B_{11} = B_{32} = 1.0 \quad (\text{B-25})$$

$$B_{22} = -3.88q_1^1 \quad (\text{B-26})$$

$$B_{12} = B_{21} = B_{31} = B_{41} = B_{42} = 0 \quad (\text{B-27})$$

Distribution

- 1 MS0439 D.R. Martinez, 9234
- 1 MS0439 C. R. Dohrmann, 9234
- 1 MS0439 B. Driessen, 9234
- 3 MS0439 G.R. Eisler, 9234
- 1 MS1003 R.D. Robinett, 9611
- 2 Gordon Parker, Michigan Tech. University, Houghton, Mich. 49931

- 1 MS9018 Central Technical Files, 8940-2
- 5 MS0899 Technical Library, 4414
- 2 MS0619 Review & Approval Desk, 12690
For DOE/OSTI
- 1 MS0188 LDRD Office